RSC Advances

PAPER

View Article Online
View Journal | View Issue

Cite this: *RSC Adv.*, 2025, **15**, 14929

Removal assessment of malathion and dichlorodiphenyltrichloroethane pesticides from wastewater using intercalated bentonite clay with mixed aluminum–zinc oxides nanoparticles

Ahmed S. M. Ali,[a] Elhassan A. Allam,[a] Gehan M. Nabil,[b] Mohamed E. Mahmoud[c] and Rehab M. El-Sharkawy *[d]

The presence of agrochemical residues in wastewater resources has raised high concerns owing to their hazardous impacts on the human health and integrity of ecosystems. In this regard, a cost-effective and readily available nanocomposite was designed and assembled *via* the combination of nano-bentonite (N-Bent), nanoalumina (NAl_2O_3), and nanozinc oxide (NZnO) for the formation of N-Bent-NAl_2O_3-NZnO. This nanocomposite was developed to remove two specific pesticides, namely, malathion and dichlorodiphenyltrichloroethane (DDT), which are frequently detected in surface water from polluted wastewater samples. The characterization of the as-synthesized N-Bent-NAl_2O_3-NZnO nanocomposite was performed using SEM, XRD, HR-TEM, FTIR, BET and TGA techniques. SEM and HR-TEM investigations revealed a favorable degree of homogeneity and surface porosity, with an average particle size of 69.8–86.9 nm. The potential use of this nanocomposite for pesticide pollutant removal was evaluated under diverse conditions *via* a batch adsorption approach. At pH 3.0, the highest observed removal (*R*%) rate was 97.42% for malathion and 94.83% for DDT. These results revealed that N-Bent-NAl_2O_3-NZnO exhibited a significantly greater overall removal efficiency for malathion than for DDT. The Langmuir model demonstrated $R^2 = 0.997$ and 0.991 for malathion and DDT, respectively. Besides, the pseudo second order model exhibited $R^2 = 0.997$ for malathion and 0.995 for DDT, indicating that these were the most suitable isotherm and kinetic model. According to the Langmuir model, the maximum removal capacities were 34.20 mg g^{-1} for malathion and 28.36 mg g^{-1} for DDT. Additionally, the effectiveness of N-Bent-NAl_2O_3-NZnO in removing malathion and DDT after five repeated adsorption–desorption cycles was achieved as 84.63% and 81.76%, respectively. These results suggest that N-Bent-NAl_2O_3-NZnO could serve as a viable and effective nanocomposite for treating wastewater generated from agricultural activities.

Received 29th January 2025
Accepted 17th April 2025

DOI: 10.1039/d5ra00683j

rsc.li/rsc-advances

1. Introduction

Water is a vital resource and a key input in numerous human activities, including the production of beverages and food, pharmaceuticals, agrochemicals, electronics, and domestic applications. Nevertheless, the release of contaminated water from these sectors significantly contributes to water pollution.[1,2] In this context, the contamination of water resources due to pesticide residues is viewed as a major environmental issue as these harmful contaminants possess carcinogenic effects even at minimal concentrations.[3]

Pesticides are either naturally occurring or artificially produced substances utilized for the purpose of controlling or eradicating pests, thereby improving agricultural yield. Currently, the worldwide application of pesticides has risen significantly, driven by the swift progress of global population and the corresponding demand for food supplies. This surge has resulted in advancements in agriculture and an increase in the variety of plant pests.[4] It has been recorded that around 2.4 million tons of active pesticide constituents are utilized globally each year.[5] The widespread use of pesticides has resulted in a substantial level of contamination, which is evident throughout all the components of the ecosystem.[6] The presence of this contamination introduces multiple health risks to both the general public and non-target ecological species because of the occasionally toxic, stable, and insoluble active components

[a]*Nuclear Power Plants Authority (NPPA), P.O. Box 11381, Cairo, Egypt*
[b]*Department of Chemistry, College of Science and Humanities in Al-Kharj, Prince Sattam Bin Abdulaziz University, Al-Kharj, 11942, Saudi Arabia*
[c]*Faculty of Science, Chemistry Department, Alexandria University, P.O. Box 426, Ibrahimia, 21321, Alexandria, Egypt*
[d]*Faculty of Dentistry, Chemistry Department, Pharos University in Alexandria, P.O. Box 37, Sidi Gaber, Alexandria, Egypt. E-mail: rehab.mansour@pua.edu.eg; Tel: +002-01229727752*

found in pesticide formulations.[7] The World Health Organization has appropriately categorized these active components into various hazardous classes: class A1 for extremely hazardous, class 1B for highly hazardous, class 2 for moderately hazardous, and class 3 for slightly hazardous.[8] The UNEP Governing Council has acknowledged 12 persistent organic pollutants (POPs) and hazardous substances, especially pesticides, with a particular emphasis on pesticides, along with the necessary regulations aimed at safeguarding human health and the environment.[9] A pivotal investigation into the environmental consequences of pesticide use was published in 1962, marking one of the earliest and most important studies in this field.[10] Considering the confirmed detrimental effects of pesticides on both water resources and the environment, researchers have endeavored to decrease their application and to remediate these substances from water sources.[11]

Organophosphorus pesticides (OPPs) represent approximately 34% of the total pesticides manufactured and distributed globally.[12] The predominant OPPs employed in agricultural practices may persist on the surfaces of plants or within the soil, resulting in environmental degradation and presenting toxic risks to plants, animals, and humans alike.[13] Malathion, scientifically known as diethyl 2-[(dimethoxyphosphorothioyl)sulfanyl]butanedioate, is a prominent OPP that is recognized for its high toxicity. Studies have revealed that its concentration in surface water can vary from ng L^{-1} to μg L^{-1}.[12] This substance exhibits particular fumigation properties and is frequently employed in the management of pests affecting tobacco, tea, mulberry, and a range of other agricultural products.[13] In alkaline conditions, the hydrolysis of malathion may result in the generation of highly toxic intermediates in aquatic systems, such as *O*,*O*-dimethyl phosphorodithioic acid, diethyl thiomalate, malaxon, diethyl fumarate, and malathion's alpha and beta monoacid derivatives.[14] The serious threat this pesticide presents to human health is attributed to its influence on cholinesterase activity, its potential to cause central nervous system disorders, its detrimental effects on the immune system, liver, and adrenal glands, and its carcinogenic characteristics.[13,14] Considering recent developments, the FDA and the EPA have implemented strict regulations concerning the use of pesticides, with a specific emphasis on malathion. The imposition of rigorous guidelines on subsequent environmental releases has prompted comprehensive monitoring of these toxins within ecological systems.[15] Alternatively, dichlorodiphenyltrichloroethane (DDT) ranks among the most prevalent OCPs and is designated as a persistent organic pollutant because of its resilience to degradation and its potential for long-distance movement.[16] Typically, the DDT compound is often noted for its considerable volatility and minimal vapor pressure, allowing it to be readily absorbed by sediment particles while demonstrating strong biodegradation resilience.[17] In addition, the lipophilic nature of DDT residual waste promotes its tendency to accumulate in the fatty tissues of the kidneys and liver, leading to disorder-related issues in humans, animals, and fish.[18] In light of the environmental degradation linked to its long-term persistence in surface water and soil for approximately 25 years, the EPA identified it as a primary pollutant and enacted a ban on its use 50 years ago.[19] Thus, the process of removing pesticide residues from wastewater using innovative technologies, along with a sustainable and economically viable strategy, has received extensive focus.[20–23]

Developing a unified and universal approach for pesticide remediation presents significant challenges.[24] The extensive range of chemical, physical, and biological approaches investigated to address pesticide pollution highlights this concern. These approaches encompass photocatalytic degradation, biodegradation, flocculation/coagulation, electrochemical and aerobic degradation, advanced oxidation, adsorption, and membrane and nanofiltration techniques.[25–31] However, most remediation technologies are characterized by their lack of versatility, significant expenses, diminished efficacy, and risk of generating secondary contaminants.[32] Numerous techniques have been recently implemented to remove organic contaminants such as DDT and malathion from water. These techniques are based on biodegradation, hydroponic, remediation and adsorption. The process of adsorption is recognized as a proficient approach for wastewater treatment, employed by various industries to reduce the levels of toxic organic and inorganic pollutants in their effluent.[33] The advantages of adsorption technique are related to their simplicity, low-cost and easy application with a great number of materials, including adsorbents, biosorbents and nanosorbents.[34] Since adsorption is a fundamental surface reaction, the effectiveness of the adsorption process depends on the physicochemical properties of the adsorbate and adsorbent.[35] Therefore, researchers have indicated that adsorption is a promising approach for the successful removal of different pollutants.[33,34] Several adsorbents have undergone testing to assess their effectiveness in removing malathion and DDT pollutants, including but not limited to activated carbon, zeolite, diatomite, polymers, and nanomaterials.[20,36–39] However, the disadvantages of adsorption techniques are sometimes related to their low efficiency and selectivity.

The recent focus on water treatment using engineered nanomaterials as nano-adsorbents highlights their considerable treatment capabilities. The production of such materials is becoming increasingly efficient, requiring fewer resources and generating less waste. These measures play a vital role in global pollution reduction initiatives.[40] Within the spectrum of nanostructures, nano-bentonite-based materials are particularly advantageous for the wastewater remediation of organic pollutants. In addition, it holds significant importance as a natural scavenger of pesticides. Their appeal lies in their specific surface area, remarkable chemical stability, outstanding adsorption and ion exchange capabilities, and affordability relative to activated carbon.[41] Previous studies involved the intercalation of nano-bentonite clay with various metal oxide nanoparticles, including ZnO NPs, Al_2O_3 NPs, and Fe_3O_4 NPs, which proved efficacy in adsorbing heavy metal ions like Cr(III), Cu(II), Pb(II), Ni(II) ions from aqueous environments.[42–44] The removal of trace amounts of Fe(II) associated with the galvanized pipe manufacturing sector[45] and Cr(III) from wastewater[46] was achieved through the

application of modified bentonite nano-clay. Nevertheless, there is a limited amount of data available regarding the possible application of this specific type of nano-clay for the separate capturing of Malathion and DDT from aqueous environments. Taking into account the considerations outlined above, it is highly pertinent to evaluate the effectiveness of locally sourced nano-bentonite intercalated with two types of metal oxide nanoparticles, specifically NZnO and NAl_2O_3, for the removal of the two mentioned pesticides from aquatic environments. The batch adsorption method was conducted while varying several experimental conditions, including pH levels, contact time, N-Bent-NAl_2O_3-NZnO dosage, and the initial concentration of the pesticide. The study encompassed an analysis of multiple kinetic models, such as first order and second order equations, the Elovich Model, the Boyd Model, and the intra-particle diffusion model, from which the corresponding parameter values were determined. In addition, this study explored the implementation of Temkin, Freundlich, and Langmuir isotherm models to characterize the adsorption process of N-Bent-NAl_2O_3-NZnO. The cost-effectiveness of the proposed method is mainly related to the production of the target nanomaterial from low-cost precursors such as aluminum ammonium sulfate dodecahydrate, zinc acetate dihydrate, and bentonite, as well as sodium hydroxide and urea. Moreover, the methods applied for the synthesis of N-Bent-NAl_2O_3-NZnO are based on both co-precipitation and combustion processes. Finally, the assembled nanocomposite can be easily accepted and transferred from laboratory to industrial scale.

2. Experimental details

2.1. Materials and chemicals

$Al(NH_4)(SO_4)_2 \cdot 12H_2O$ (FW 453.3 g mol^{-1} and >99.0%), HCl (FW 36.5 g mol^{-1} and 37%), and CH_3OH (FW 32.04 g mol^{-1} and >99.8%) were acquired from Sigma-Aldrich Company, USA. $CO(NH_2)_2$ (FW 60.0 g mol^{-1} and >99.0%) was obtained from Oxford Company, India. $Zn(CH_3COO)_2 \cdot 2H_2O$ (FW 219.6 g mol^{-1} and >98.5%) and C_2H_5OH (FW 46.07 g mol^{-1} and >99.8%) were purchased from BDH, UK. NaOH (FW 40.0 g mol^{-1} and >99%) was procured from Merck, Germany. Bentonite ($H_2Al_2O_6Si$, FW 180.1 g mol^{-1} and >95%) was provided by Sigma-Aldrich, USA, and the material was processed through intensive grinding with a ball milling machine, facilitating its transformation into nano-bentonite. Malathion and DDT of analytical grade, possessing a chemical purity exceeding 99%, were supplied by Sigma-Aldrich, USA, and as received. Table 1 lists the chemical structures and physicochemical properties of the malathion and DDT pesticides.

2.2. Instrumentation

Various instrumentations, *viz.* FT-IR, TGA, XRD, HR-TEM, BET and SEM, were employed to conduct the structural and surface identification of the N-Bent-NAl_2O_3-NZnO nanocomposite. The instrumentation details of the characterization techniques used in this study are presented in Table 2.

2.3. Synthesis

2.3.1. Synthesis of aluminum oxide nanoparticles (NAl_2O_3). NAl_2O_3 was synthesized using a straightforward combustion method.[47] In the course of this process, 22.5 g of $Al(NH_4)(SO_4)_2 \cdot 12H_2O$ were entirely dissolved in a volume of 100 mL of double distilled water. Subsequently, 100 mL of NaOH at a concentration of 1.5 M was gradually introduced into the solution while maintaining continuous stirring until the development of a white precipitate of $Al(OH)_3$ was observed. Following precipitate production, the precipitate was separated *via* the process of filtration and rinsed with double distilled water. The precipitate was slowly heated at 60 °C for 6 h to ensure proper drying. The subsequent step involved the blending of $CO(NH_2)_2$ and $Al(OH)_3$ in a 1 : 1 stoichiometric ratio using double distilled water at a temperature of 80 °C. Continuous stirring was maintained throughout this process until a paste was obtained. The paste was allowed to dry for 24 h at 120 °C. After this drying period, the sample was subjected to calcination for 6 h at 900 °C in a muffle furnace. The substance was allowed to cool in a desiccator. Ultimately, it was processed with an agate pestle and mortar to obtain NAl_2O_3.

2.3.2. Synthesis of zinc oxide nanoparticles (NZnO). Following the methodology outlined by Mahmoud *et al.*,[48] a basic combustion approach was used for the synthesis of NZnO. A total of 100 mL of 0.5 M NaOH solution was gradually added to 500 mL of a 0.05 M solution of zinc acetate dihydrate. The solution was heated with stirring for 90 min at 80 °C to form a white precipitate. The resulting $Zn(OH)_2$ precipitate was separated by decantation, washed three times and dried overnight at 70 °C. Following the acquisition of the final product, distilled water was employed to blend the designated stoichiometric quantities of $CO(NH_2)_2$ and $Zn(OH)_2$, while stirring at 80 °C until a paste consistency was achieved. The resulting mixture was dried at 70 °C for 24 h. To generate NZnO, the dried mixture was heated to 500 °C for a duration of 6 h.

2.3.3. Synthesis of the N-Bent-NAl_2O_3-NZnO nanocomposite. The N-Bent-NAl_2O_3-NZnO nanocomposite was synthesized *via* a specific procedure. To begin, 2.0 g of nano-bentonite clay underwent activation by being ultrasonically dispersed in 100 mL of a 0.001 M NaOH solution for 30 min at 65 °C. After completing this step, an equal weight of 2.0 g of each of the as-synthesized metal oxides (NZnO and NAl_2O_3) was progressively added to the N-Bent suspension. Continuous stirring was maintained to ensure thorough dispersion and intercalation of the designated metal oxide nano-powders within the nano-bentonite clay layers. The mixture was subsequently subjected to heating at 90 °C for 90 min, during which all water was evaporated, yielding a paste composed of N-Bent-NAl_2O_3-NZnO. The paste was allowed to dry thoroughly in an electric furnace adjusted to 60 °C for 24 h. The end product was processed into an extremely fine powder.

2.4. Gas chromatography analysis (GC-MS)

The assessment and quantification of the equilibrium concentrations of malathion and DDT within a solution were carried out through the use of the Agilent 7890A Gas

Table 1 Physicochemical properties of malathion and DDT

Parameter	Malathion	DDT
IUPAC name	Diethyl 2-[(dimethoxyphosphorothioyl)sulfanyl]butanedioate	1,1-(2,2,2-Trichloroethane-1,1-diyl) bis(4-chlorobenzene)
Structural formula	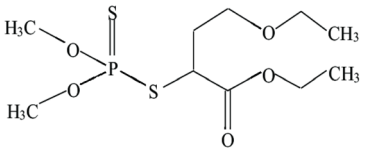	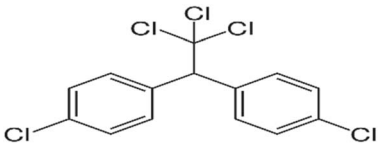
Molecular formula	$C_{10}H_{19}O_6PS_2$	$C_{14}H_9Cl_5$
Function	Insecticide	Insecticide
Molecular weight	330.36 g cm^{-3}	354.49 g cm^{-3}

Chromatography System along with an Agilent 5975C Triple-Axis Mass Detector (GC-MS). For pesticide detection, an HP-5MS UI capillary column characterized by 0.32 mm id, 0.25 μm film thickness, and length of 30.0 m was employed. The analysis assays were conducted using gas chromatography technologies that employed vials with a volume of 1.5 mL, which were fitted with septum screw caps. For the temperatures, the column was adjusted accordingly: the oven was set to an initial temperature of 80 °C, which was held for 0 min. An increase in the temperature of 30 °C per minute was implemented to achieve a final temperature of 178 °C, which was sustained for 4 min. The temperature was then increased by 2 °C per minute until it reached 205 °C, which was maintained for 0 min. The injector was established at a temperature of 260 °C, while the mass spectrometer interface was configured to 300 °C, and the flow of the helium carrier gas was maintained at 0.5 mL min^{-1}. In the process of compound identification, each mass spectrum captured within the m/z range of 50.0–500.0 amu was scrutinized against the library available in Agilent MSD Chemstation software®.[33] Individual 1000.0 mg L^{-1} stock solutions of malathion and DDT were prepared in 100.0 mL volumetric flasks. This process was accomplished by the dissolution of 100.0 mg of each targeted organic contaminant (Malathion and DDT) in acetone, followed by filling the flask with the designated volume mark. Sequential dilutions of this solution were performed to obtain reduced concentrations that were appropriate for testing. The standard solutions and prepared samples were protected from light exposure and were stored in a dark area at 4 °C until they were required for subsequent use.

Table 2 Instruments used and their specifications

Instrument name	Model	Data	Conditions
Fourier-transform infrared spectrophotometer FT-IR	A BRUKER VERTEX 70	FT-IR spectrum	400–4000 cm^{-1}
TGA-7 thermobalance	A Perkin–Elmer	Thermogram	Pure atmospheric nitrogen, flow rate = 40 mL min^{-1}, heating rate = 10 °C min^{-1}, sample mass in the range of 5.0–6.0 mg, heating temperature 25–800 °C
X-ray diffraction (XRD)	Shimadzu Lab x 6100, Kyoto, Japan	XRD spectrum	The XRD generator works at 40 kV, 30 mA, $\lambda = 1$ Å, using target Cu-Kα with secondary monochromatic X-ray, 2θ from 10° to 80°, recording steps of the diffraction data of 0.02°, at a time of 0.6 s, at room temperature (25 °C)
Scanning electron microscope (SEM)	JSM-lT200, JEOL Ltd, Sputtering coating (JEOL-JFC-1100E)	SEM images	Imaging mode
High resolution Transmission electron microscope (HR-TEM)	JEOL- JSM-1400 plus	TEM image	Imaging mode
Brunauer–Emmett–Teller (BET) surface area	BELSORP-mini II, BEL, Japan	Surface area, pore volume and pore size distribution	The required data were determined by nitrogen adsorption–desorption isotherm measurements at adsorption temperature 77 K and saturated vapor pressure of 100.25 kPa for 24 h

2.5. Adsorption of malathion and DDT by the N-Bent-NAl_2O_3-NZnO nanosorbent

The adsorption characteristics of malathion and DDT by the N-Bent-NAl_2O_3-NZnO nanosorbent from an aquatic medium were analyzed through the application of the batch adsorption technique. This study analyzed and optimized the effects of diverse parameters applied throughout the adsorption process. The parameters considered were the initial pH, pollutant concentration, contact time and nanocomposite mass dose. Each experiment was executed at a controlled room temperature of 25 ± 1.0 °C using Stoppard Pyrex bottles of 10.0 mL capacity, with a consistent shaking speed of 240 rpm. To analyze the influence of initial pH, 40.0 mg of N-Bent-NAl_2O_3-NZnO was added to 10.0 mL of a 40.0 mg L^{-1} malathion or DDT solution. The initial pH values varied from 1.0 to 11.0. To achieve the desired pH levels in the tested solutions, drops of 0.1 M HCl or 0.1 M NaOH were incorporated into the mixture. The suspension was then subjected to automatic stirring by a mechanical shaker set at 240 rpm for 80 min to ensure the achievement of equilibrium. Subsequently, the supernatant liquid was passed through a 0.22 mm polypropylene syringe filter, and the concentrations of malathion or DDT in the solution were measured before and after the equilibrium adsorption process using GC-MS analysis. The previous steps were carried out three times, and the average R% representing the removal efficiency of N-Bent-NAl_2O_3-NZnO for the selected pollutants can be determined by eqn (1):

$$\% R = \frac{(C_o - C_e)}{C_o} \times 100 \quad (1)$$

where C_o is the initial concentration of malathion and DDT expressed in mg L^{-1}, and C_e is the concentration of malathion and DDT once equilibrium has been reached. Moreover, the equilibrium concentration of the adsorbed pollutants, represented as q_e (mg g^{-1}), was ascertained through the application of eqn (2):

$$q_e = \left(\frac{C_o - C_e}{W}\right) \times V \quad (2)$$

where W denotes the mass of N-Bent-NAl_2O_3-NZnO, given in grams (g), and V denotes the working solution volume, quantified in liters (L).

The shaking duration and its influence on the adsorption of malathion and DDT were conducted in the following manner: a volume of 10.0 mL of malathion or DDT solution at 40.0 mg L^{-1} was added to 40.0 mg of N-Bent-NAl_2O_3-NZnO samples contained in Stoppard Pyrex bottles. Subsequently, the solution pH was calibrated to match the optimal value identified in step 1. After completing this step, the reaction mixture was subjected to automatic shaking for durations of 10–120 min. The solution mixtures were subsequently filtered, and the remaining concentration was determined as previously described. After the designated time intervals, the concentrations of malathion and DDT were measured, and the capacity at a specific time t, indicated as q_t (mg g^{-1}), was calculated using eqn (3).

$$q_e = \left(\frac{C_o - C_t}{W}\right) \times V \quad (3)$$

where C_t (expressed in mg L^{-1}) is the malathion and DDT concentrations in the liquid phase at the specified equilibrium time t (measured in min). In the end, the determination of the values of R% was determined using eqn (1). The outcomes derived from this section served as a basis for investigating the kinetic models, focusing on the rates and interaction mechanisms of N-Bent-NAl_2O_3-NZnO.

The impact of varying doses of N-Bent-NAl_2O_3-NZnO on the removal efficiency of malathion and DDT from aqueous environments was investigated by employing different masses of the nanocomposite, ranging from 20.0 to 120.0 mg. All other experimental parameters, including the optimal solution pH, initial pollutant concentration, and shaking duration, were held constant. The designated mass was combined with 10.0 mL of a 40.0 mg L^{-1} solution of either malathion or DDT and subjected to shaking for 80 minutes. The subsequent adsorption procedures were performed as previously detailed, and the R% values were computed using eqn (1). The quantities of adsorbed substances at equilibrium, denoted as q_e (mg g^{-1}), were derived from eqn (3).

The impact of malathion and DDT concentrations on the adsorption process was examined in a concentration range of 10.0–100.0 mg L^{-1}. A mixture was prepared by combining 40.0 mg of N-Bent-NAl_2O_3-NZnO with 10.0 mL of the designated concentrations of either malathion or DDT solutions. The R% values for malathion and DDT were computed according to eqn (1). The outcomes of the factor of concentration were applied to examine the adsorption isotherm concerning the removal of malathion and DDT from N-Bent-NAl_2O_3-NZnO through the application of various models.

An assessment of the reusability and regeneration of N-Bent-NAl_2O_3-NZnO was performed through a series of adsorption–desorption-re-adsorption processes. This process was conducted over five cycles at room temperature using a mixture of methanol (MeOH) and acetic acid (HAc) in a volume ratio of 9 : 1 as the desorption eluent. The procedure involved the mixing of 100.0 mg of N-Bent-NAl_2O_3-NZnO with 10.0 mL of malathion or DDT (40.0 mg L^{-1}) to achieve saturated adsorption. The pH was set to 3.0, and the samples were shaken at room temperature for 80 min. The next step involved the filtration and separation of N-Bent-NAl_2O_3-NZnO, along with the targeted organic pollutants in the solution. A sufficient mixture of MeOH and HAc was used to elute the adsorbed malathion or DDT. The remaining mass of N-Bent-NAl_2O_3-NZnO was washed multiple times with double distilled water, followed by acetone. Then, this mass was allowed to air dry at room temperature. Upon completion of each adsorption cycle, the supernatant obtained was analyzed, and the effectiveness of the re-adsorption was assessed following the previously outlined methodology. To evaluate the performance of the recycled N-Bent-NAl_2O_3-NZnO nanosorbent in the removal of malathion or DDT, the adsorption experiment was replicated no fewer than five times employing solutions of organic pollutants that maintained the same concentration. The synthesized Bent NAl_2O_3-NZnO nanocomposite was

characterized by high chemical, thermal, and mechanical stability and these incorporated characteristics make the investigated nanocomposite acceptable for implementation in real wastewater treatment. In addition, this study focused on the removal of malathion and DDT pesticides from aquatic systems. However, other organic contaminants are expected to interfere with or be removed by Bent NAl_2O_3-NZnO nanocomposite.[49–52]

3. Results and discussion

3.1. Characterization of N-Bent-NAl_2O_3-NZnO nanocomposite

To confirm the successful assembly of the targeted N-Bent-NAl_2O_3-NZnO nanocomposite, FT-IR analysis was conducted. Fig. 1a displays the FT-IR spectrum of NZnO, which shows six prominent peaks at 1437.17, 1552.44, 687.32, 864.88, 415.01 and 902.75, cm^{-1}. The peak at 415.01 cm^{-1} corresponds to the stretching vibration of the Zn–O bond, confirming the successful synthesis of the final product.[48] The presence of moisture led to two bands around 1437.17 and 3630.21 cm^{-1}, attributed to the stretching and bending vibrations of H–O–H, respectively.[34] Furthermore, the significant peak at 1552.44 cm^{-1} indicates a robust metal–oxygen bond in ZnO. Additional weaker bands were observed at 864.88, 687.32 and 902.67 cm^{-1}, which are associated with the ZnO nanoparticles.[48] Regarding NAl_2O_3 (Fig. 1b), three peaks were identified at 636.28, 434.68, and 494.12 cm^{-1}, which are related to the Al–O–Al stretching vibration.[47] The FT-IR spectrum of N-Bent (Fig. 1c) exhibited weak absorption peaks at 1648.09 and 3451.89 cm^{-1}, signifying the bending and stretching vibrations of –OH, respectively, due to physically adsorbed water molecules.[42] Moreover, a distinct peak at 1035.63 cm^{-1} is clear in the silicate structured clay material, indicating the presence of Si–O.[33] Two additional peaks are noted, corresponding to the typical bentonite form at 458.22 and 527.15 cm^{-1}, which is associated with the vibration of octahedral Al–O–Si and bending Si–O–Si. The presence of out-of-plane vibrations for Si–O and Al–O was evidenced by the weak peak at 797.32 cm^{-1}.[42] Furthermore, the peak at 3631.08 cm^{-1} signifies the hydroxyl groups associated with Al^{3+} cations.[33]

The FT-IR spectrum of N-Bent-NAl_2O_3-NZnO is shown in Fig. 1d, and the figure shows the presence of the characteristic peaks of all the functional groups of the nanocomposite constituents with a slight shift in wavenumber. The weak band identified at 3777.12 cm^{-1} corresponds to –OH groups associated with the octahedral Al^{3+} cation found in the nano-bentonite segment of the synthesized N-Bent-NAl_2O_3-NZnO nanocomposite.[42] The presence of another notable peak in nano-bentonite is observed at 1101.66 cm^{-1}, which is linked to the Si–O in-plane vibrations, thereby illustrating the silicate composition of bentonite clay. Additionally, the peak at 554.96 cm^{-1} is related to the bending vibrations of Si–O–Si, while the peaks identified at 422.49 cm^{-1} are indicative of Si–O–Al octahedral vibrations.[33] The weak bands noticed at 698.52 and 901.83 cm^{-1} correspond to asymmetric O–Si–O bonds. The moderate peak at 1635.75 cm^{-1} and the broad band at 3365.45 cm^{-1} are linked to –OH groups, respectively, resulting from the presence of adsorbed water molecules onto the N-Bent-NAl_2O_3-NZnO nanosorbent.[35] Conversely, the peaks recorded at 774.62, 653.79, and 803.13 cm^{-1} are assigned to the symmetric stretching vibrations of nano-metal oxides, specifically Zn–O–Zn and Al–O–Al. This finding substantiates the successful intercalation of both NAl_2O_3 and NZnO within the layers of nano-bentonite clay in the reaulting N-Bent-NAl_2O_3-NZnO nanocomposite.[47,48] The information presented in Fig. 1d suggests that the presence of multiple peaks linked to the functional groups of the nanocomposite's components, namely nano-bentonite, NAl_2O_3, and NZnO, serves as a definitive indication of the successful fabrication of N-Bent-NAl_2O_3-NZnO.

The X-ray diffraction patterns for NAl_2O_3, NZnO, N-Bent and the corresponding N-Bent-NAl_2O_3-NZnO nanocomposite are illustrated in Fig. 2. The XRD pattern of NZnO is illustrated in Fig. 2a, showing the peaks corresponding to Bragg's reflections at 2θ = 31.61°, 34.25°, 36.64°, 47.95°, 56.22°, 62.88°, 66.39°, 67.78°, and 68.99°. The planes associated with these reflections were identified as (100), (002), (101), (102), (110), (103), (200), (112), and (201), respectively.[48] Such a diffraction pattern substantiates the identification of a ZnO hexagonal wurtzite structure, as referenced by the JCPDS card 36-1451.[48] The distinct intensity and sharpness of these peaks indicate the crystalline quality of the prepared NZnO. Furthermore, the high purity of the synthesized product is evident because of the absence of diffraction peaks for the impure derivatives. The XRD pattern of NAl_2O_3 shows distinct peaks (Fig. 2b). These peaks are positioned at 2θ = 35.14°, 37.78°, 43.34°, 57.5°, 61.26°, and 66.50°, respectively. The corresponding Miller indices for Bragg's peaks are (220), (222), (400), (311), (511), and (440) planes, respectively. These diffraction patterns indicate aluminum oxides with a cubic face-centered structure.[47] The diffraction pattern of N-Bent is shown in Fig. 2c and displays a series of peaks at 2θ = 20.8°, 25.6°, 28.1°, 35.8°, 38.3°, and 55.3°, which correspond to the crystallographic planes (110), (210), (124), (144), (102), and (220), respectively. This pattern aligns with JCPDS Card No. 01-088-0891 for raw bentonite, confirming the presence of these peaks.[42] The diffraction peaks identified in the analysis revealed the existence of an aluminum silicate structure in the nano-bentonite sample, which was characterized by its amorphous features to affirm that the sample mainly consisted of montmorillonite (M) hexagonal form, quartz (Q) trigonal configuration, and feldspar (F) with an albite structure, marking it as the predominant clay mineral.[33] The X-ray diffraction pattern of N-Bent-NAl_2O_3-NZnO is presented in Fig. 2d, highlighting the amorphous characteristics of this nanocomposite, as evidenced by the absence of sharp peaks. The examination of the diffractogram indicates the existence of several XRD peaks corresponding to NZnO, NAl_2O_3, as well as N-Bent, which appeared at their expected positions and in accordance with their respective quantities. This confirms the successful intercalation of both NZnO and NAl_2O_3 nanoparticles into the N-Bent clay matrix.

Fig. 3 presents the TGA thermogram of the developed N-Bent-NAl_2O_3-NZnO nanocomposite. It is noteworthy that the thermogram shows three distinct minor thermal degradation

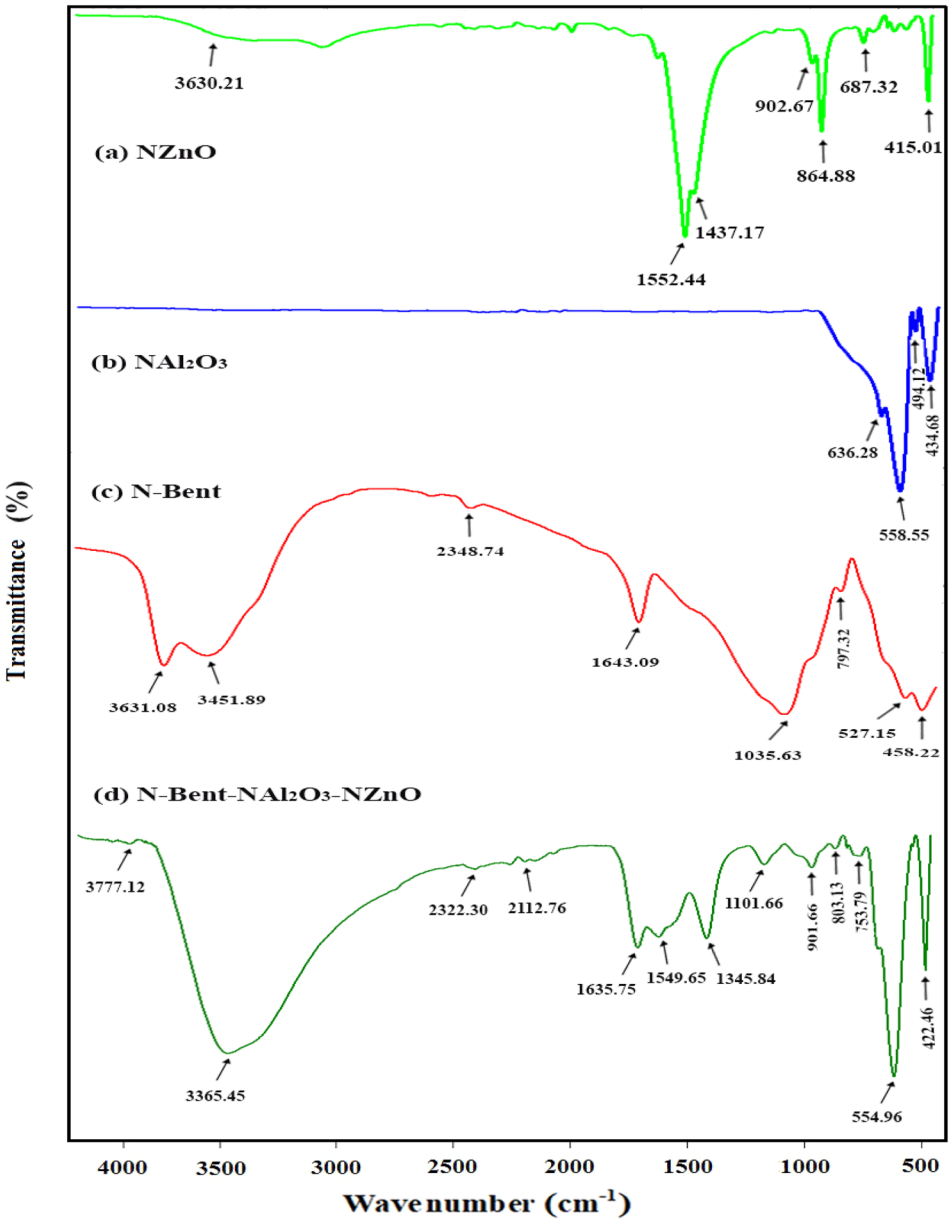

Fig. 1 FT-IR spectra of (a) NZnO, (b) NAl_2O_3, (c) N-Bent, and (d) the N-Bent-NAl_2O_3-NZnO nanocomposite.

steps. The first one is identified within the temperature interval of 21.10 °C to 394.51 °C, where a mass reduction of 0.688% from the initial mass of the sample is recorded, attributed to the potential evaporation of moisture adsorbed on the nanocomposite's surface.[42] In the next step, a decrease of 0.918% was observed as the temperature rose from 394.51 °C to 448.79 °C. This decline is primarily due to the evaporation of water of crystallization along with the release of internal water molecules from the intercalated N-Bent layers, particularly water lost *via* the exchange layer, which is commonly referred to as "interlayer water".[33] The final stage of thermal degradation started at approximately 448.79 °C and continued until reaching 799.87 °C, resulting in a mass loss of 0.197%. This phase is likely due to the dehydroxylation of the silicate lattice, along with the complete breakdown of the organic components found within the clay mineral framework of the assembled nanocomposite.[42] As shown in Fig. 3, the cumulative mass loss of N-Bent-NAl_2O_3-NZnO throughout the three thermal degradation steps was approximately 1.5%. This result reflects the considerable thermal stability of the prepared nanosorbent material.

The typical microstructural images of the synthesized N-Bent-NAl_2O_3-NZnO nanocomposite are shown in Fig. 4a and b, displaying the results of SEM and HR-TEM examinations. As illustrated in Fig. 4a, the SEM image of the nanocomposite reveals a rough surface characterized by semi-spherical nanoparticles composed of Al_2O_3 and ZnO. These nanoparticles were monodispersed and exhibited a uniform distribution, with minor agglomerations visible as bright areas in the SEM micrographs. The average particle size was within the nanometer scale. The characteristics of this surface morphology

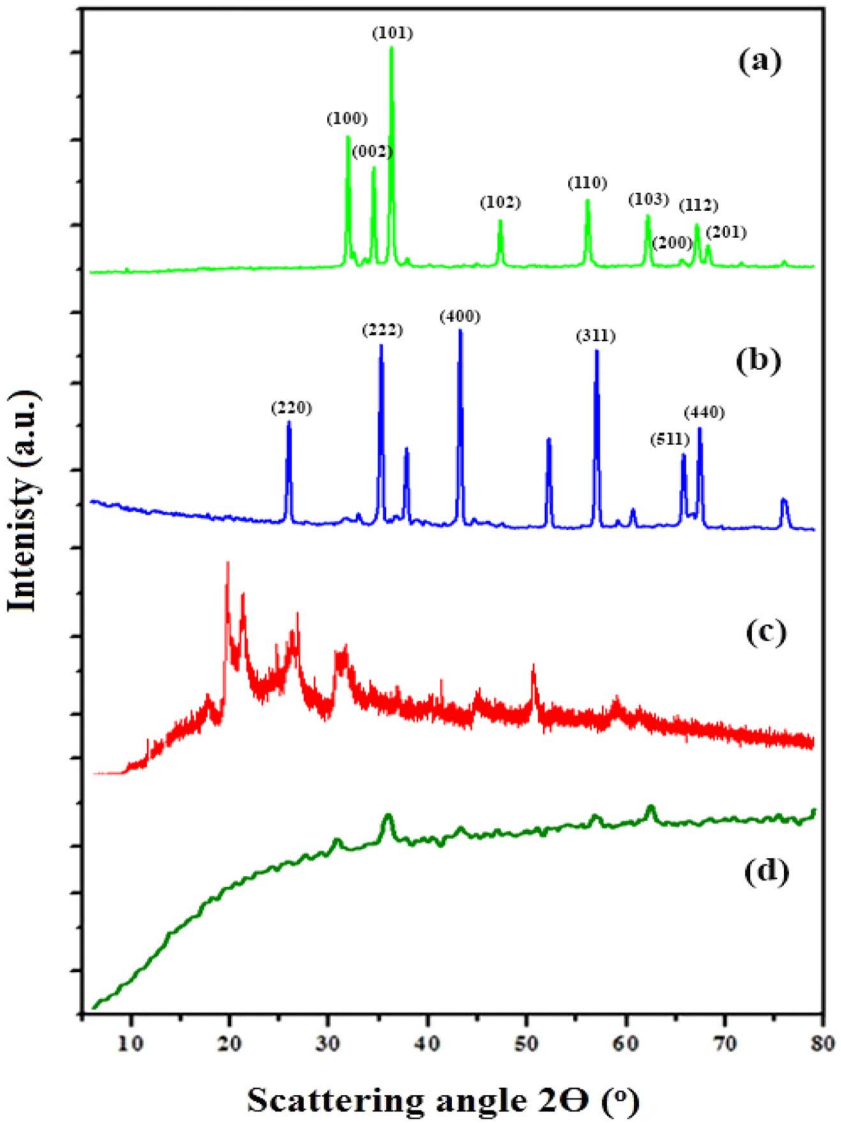

Fig. 2 XRD patterns of (a) NZnO, (b) NAl_2O_3, (c) N-Bent, and (d) the N-Bent-NAl_2O_3-NZnO nanocomposite.

provide substantial proof of the effective cross-linking among the nanocomposite, thereby validating the successful synthesis. Moreover, the SEM image (Fig. 4a) indicates that the surface of N-Bent-NAl_2O_3-NZnO has many pores, which facilitate the adsorptive binding of the targeted organic pollutants. The HR-TEM image of N-Bent-NAl_2O_3-NZnO (Fig. 4b) shows results that closely align with the conclusions drawn from the SEM analysis. The image demonstrates that the nanocomposite surface is characterized by a wrinkled appearance, with NAl_2O_3 and NZnO consistently arranged in clusters upon the bentonite clay layers, displaying an average particle size of 69.8 nm. The presence of selected metal oxide nanoparticles within the nano-bentonite clay layers is responsible for the dark spots observed in the HR-TEM image, whereas the lighter areas correspond to the clay itself.

The surface area and porosity of the N-Bent-NAl_2O_3-NZnO nanocomposite were determined using the Brunauer–Emmett–Teller (BET) method, with the corresponding nitrogen adsorption–desorption isotherm, as shown in Fig. 5. The isotherm curve of N-Bent-NAl_2O_3-NZnO shows a type IV profile, which is commonly associated with mesoporous materials, and features a type H3 hysteresis loop linked to capillary condensation within the mesopores.[33] The characterization of the N-Bent-NAl_2O_3-NZnO nanocomposite at standard temperature and pressure (STP) revealed a BET surface area of 7.6214 $m^2\ g^{-1}$, a total pore volume of 2.3568×10^{-2} $cm^3\ g^{-1}$ ($P/P_o = 0.990$), and an average pore diameter of 11.752 nm. The information from the BET measurements can also be used to determine the bulk density of N-Bent-NAl_2O_3-NZnO. The findings indicated that the bulk density of the synthesized nanocomposite samples was 2.53 g cm^{-3}.

3.2. Adsorption studies of malathion and DDT onto N-Bent-NAl_2O_3-NZnO

3.2.1. Effect of pH. The initial pH adjustment in the experimental solution serves as a vital factor in the adsorption

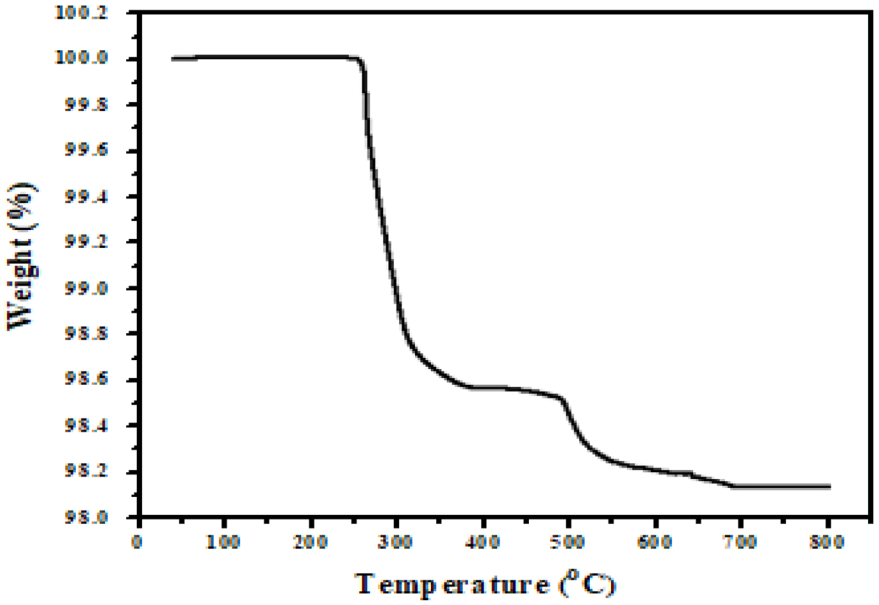

Fig. 3 TGA thermogram of the N-Bent-NAl_2O_3-NZnO nanocomposite.

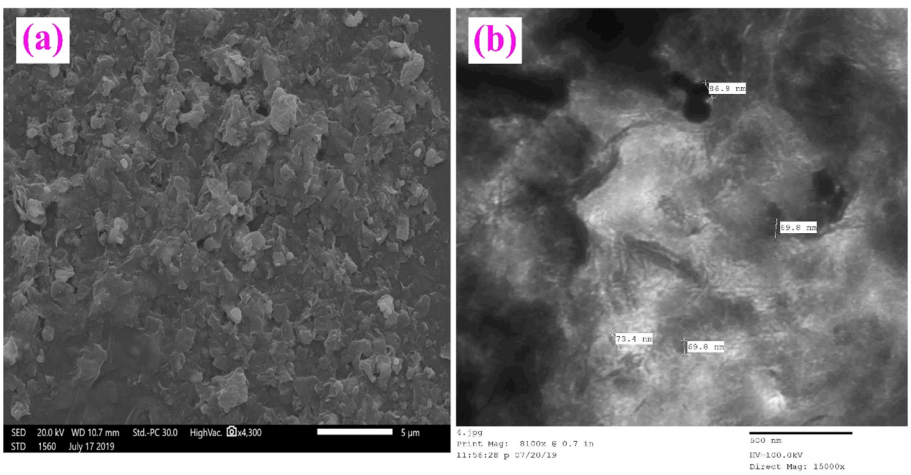

Fig. 4 (a) SEM and (b) HR-TEM images of the N-Bent-NAl_2O_3-NZnO nanocomposite.

process, impacting the ionization level of the adsorbent species, including malathion and DDT, along with the degree of surface alteration and the dissociation of functional groups at the active sites of the adsorbent (N-Bent-NAl_2O_3-NZnO). Consequently, the pH efficiency of malathion and DDT adsorption onto N-Bent-NAl_2O_3-NZnO was investigated under all pH environments—acidic, neutral, and alkaline at 25 °C using an initial concentration 40 mg L^{-1} of either malathion or DDT. The data presented in Fig. 6a indicate that the adsorption behavior of DDT closely mirrored that of malathion. The highest adsorption efficiencies (R%) for both contaminants were recorded at pH 3.0, with malathion achieving 97.42% and DDT achieving 94.83%. It is important to highlight that the adsorption tendencies for malathion and DDT are more pronounced in acidic environments (pH > 5.0), whereas a marked decrease in adsorption efficiency was recorded at pH levels exceeding 5.0. This situation may be explained by the significant concentration of H^+ ions present at reduced pH values, which effectively neutralizes the negative surface charge on the N-Bent-NAl_2O_3-NZnO nanocomposite. Comparable findings have been reported in several adsorption studies.[33,34] In contrast, at elevated pH levels, a fraction of the surface functional groups are expected to undergo increased deprotonation. This change facilitates the weak interactions between the N-Bent-NAl_2O_3-NZnO nanosorbent and the malathion and DDT substances. The relationship between pH and the adsorption of malathion and DDT on the material's surface at reduced pH values indicates that chemisorption is the primary process occurring in this range. Conversely, at higher pH levels, both chemisorption and physisorption are believed to occur. This behavior can be

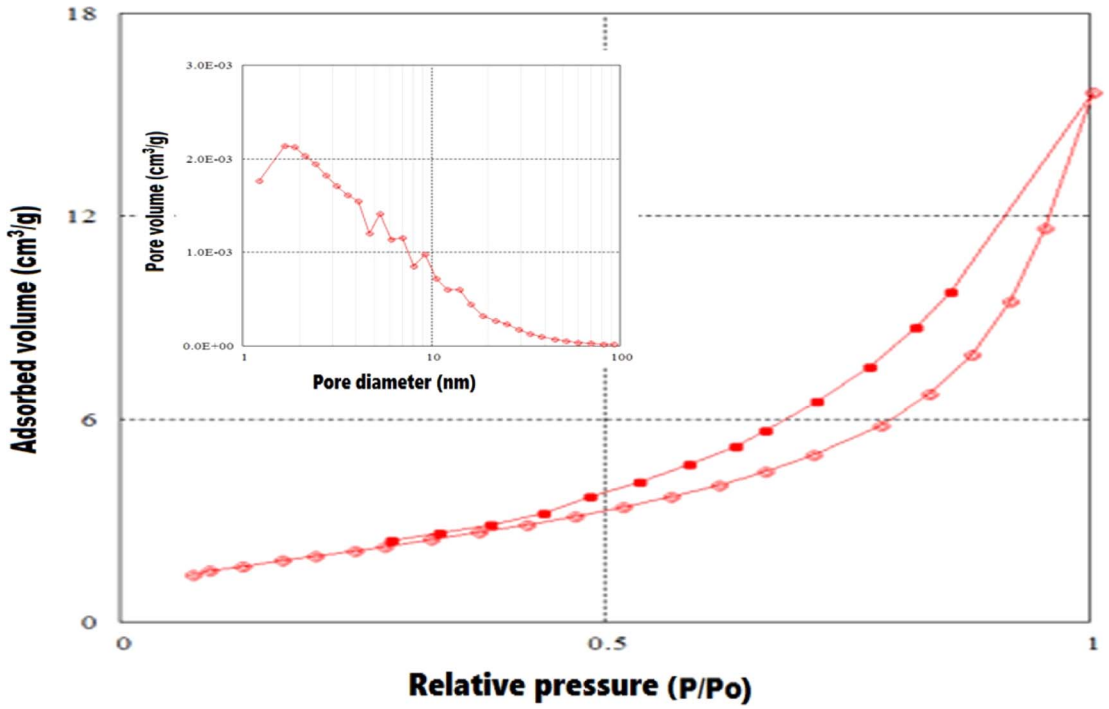

Fig. 5 Nitrogen adsorption–desorption isotherm of the N-Bent-NAl_2O_3-NZnO nanocomposite. The inset shows the pore size.

elucidated by considering the surface properties under acidic conditions and the negatively charged oxide surface of N-Bent-NAl_2O_3-NZnO.

3.2.2. Effects of contact time and kinetic evaluation. The adsorption efficiency (R%) of N-Bent-NAl_2O_3-NZnO for malathion and DDT is illustrated in Fig. 6b in relation to contact time. It is evident that, the adsorption capability improves with extended contact time, and the overall process can be divided into three sequential steps. Within the first 60 min, malathion and DDT exhibited a rapid adsorption rate. This phenomenon can be ascribed to the extensive diffusion of malathion and DDT molecules onto N-Bent-NAl_2O_3-NZnO, facilitated by a high mass transfer driving force, coupled with the adsorption sites on the nanocomposite surface at the beginning of the adsorption process.[33] The adsorption rates of malathion and DDT show a gradual reduction from 60 min to 80 min, ultimately stabilizing after the 80 min. This trend is likely due to an increase in internal diffusion resistance as the binding sites become filled. Furthermore, the partial blockage of specific active sites by malathion and DDT molecules that have already been adsorbed may also contribute to this behavior. These results imply that the adsorption equilibrium was achieved within 80 min intervals for both organic contaminants.

To explore the adsorption mechanism of N-Bent-NAl_2O_3-NZnO, multiple non-linear kinetic models were employed, specifically Lagergren's pseudo first order, Ho's pseudo second order, Weber's intra-particle diffusion, and Elovich and Boyd kinetic models, to interpret the experimental findings. Table 3 presents a summary of the non-linear equations along with the calculated parameters characteristic of mathematical kinetic models. In this table, the parameters K_1, K_2, and K_i denote the rate constants associated with the Lagergren model, pseudo second order and intra-particle diffusion expressions, respectively. Additionally, α and β signify the adsorption rate and desorption constant, which are related to the degree of nanocomposite coverage and the activation energy involved in the chemisorption reaction. The illustrations of the analyzed non-linear kinetic models are shown in Fig. 7a and b. The information in Table 3 indicates that the adsorption isotherm of malathion and DDT onto this nanosorbent aligns more closely with the pseudo second order model ($R^2 > 0.99$) than the Lagergren model. This conclusion is supported by the notable linearity and fitting of the data associated with the q_e values derived from the pseudo second order model. Moreover, the q_e value of malathion (37.20 mg g^{-1}) was greater than that of DDT (32.17 mg g^{-1}). This comparison further demonstrates the outstanding adsorption efficiency of Bent-NAl_2O_3-NZnO concerning malathion. The estimated theoretical values of q_e for malathion and DDT based on the pseudo first order kinetics were approximately 50% lower than the experimental q_e values. A plot of the computed q_e from the pseudo first order model *versus* adsorption time reveals a notable divergence between the theoretical and experimental data, suggesting that the Lagergren model fails to adequately represent the adsorption performance of malathion and DDT onto N-Bent-NAl_2O_3-NZnO. Moreover, the theoretical values of q_e, as predicted by the pseudo second order model, displayed a strong alignment with the experimental data of q_e. These results collectively suggest that the adsorption mechanisms of malathion and DDT are consistent with the pseudo second order model. In addition, the findings show limited compatibility with the Elovich kinetic model, as evidenced by the plots for the N-Bent-NAl_2O_3-NZnO

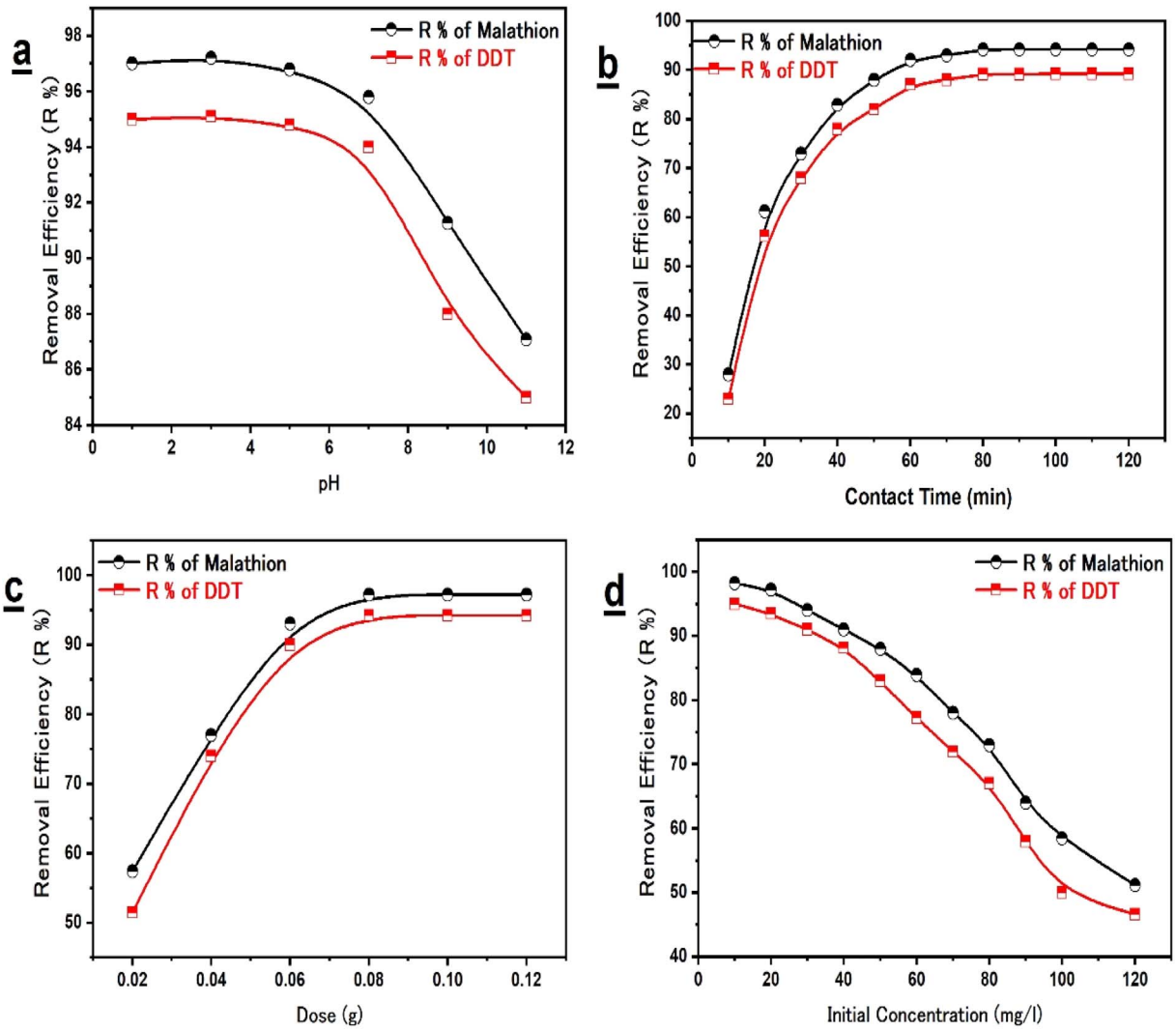

Fig. 6 Effect of (a) initial solution pH, (b) contact time, (c) nanocomposite dose, and (d) initial organic pollutant concentration on the removal efficiency (*R*%) of malathion and DDT adsorption by N-Bent-NAl_2O_3-NZnO. (Sample volume = 10.0 mL; nanocomposite dose = 40.0 ± 1.0 mg; malathion & DDT initial concentrations = 40.0 mg L; initial pH value = 3.0; shaking time = 80 min; temperature = 25.0 ± 1.0 °C; shaking speed = 240 rpm).

nanocomposite that did not intersect the origin. However, the results displayed a commendable fit with the intra-particle diffusion model. The assessment of the diffusion of malathion and DDT particles into the macro-pores of N-Bent-NAl_2O_3-NZnO was performed using the intra-particle model, which demonstrated a high correlation coefficient of $R^2 = 0.984$ for malathion and $R^2 = 0.988$ for DDT. The adsorption process, when analyzed through the lens of general intra-particle diffusion, can typically be segmented into several distinct stages. The initial stage, marked by a sharp increase, is known as external surface adsorption or instantaneous adsorption. This is followed by a progressive adsorption phase in which the intra-particle diffusion acts as the rate-limiting step. In certain instances, a third stage may emerge, referred to as the final equilibrium stage, in which the rate of intra-particle diffusion diminishes as the concentration of adsorbate in the solutions becomes exceedingly low.[34] The data illustrated in Fig. 7a and b reveal multi-linear plots. This finding implies that surface adsorption and intra-particle diffusion occur concurrently, contributing to the overall adsorption mechanism. The initial phase is likely controlled by the rate of the surface reaction. Once the quantity of adsorbed material approached approximately 90% of the equilibrium capacity, the kinetics were regulated at the rate of intra-particle diffusion. In the context of the Boyd kinetic model, B_t denotes the theoretical function corresponding to the adsorbed fractions of malathion and DDT at multiple time intervals, whereas q_α is the quantity that is adsorbed when time approaches infinity. For N-Bent-NAl_2O_3-NZnO, the theoretical equilibrium capacity, $q_{e(cal)}$, exceeded the experimental value, $q_{e(exp)}$. The analysis indicated a lack of fit to the Boyd model, signifying that malathion and DDT are primarily related to external mass transport or film diffusion mechanisms, as the plots did not originate from the zero point for the N-Bent-NAl_2O_3-NZnO nanosorbent. Thus, the findings of

Table 3 Kinetic models and their parameters for the adsorptive removal of malathion and DDT using the N-Bent-NAl_2O_3-NZnO nanocomposite

Parameter	Malathion	DDT
Pseudo first **order model** $\ln(q_e - q_t) = \ln q_e - k_1 t$		
R^2	0.718	0.801
$q_{e(cal)}$	12.41	14.17
K_1	3.17	2.65
Pseudo second **order model** $t/q_t = (1/k_2 q_e^2 + (t/q_e))$		
R^2	0.997	0.995
$q_{e(cal)}$	37.20	32.17
K_2	0.132	0.054
Intra-particle diffusion model $q_t = k_i t^{1/2} + C$		
R^2	0.978	0.962
K_{id}	3.70	2.50
C	10.27	15.14
Elovich model $q_t = \alpha + \beta \ln t$		
R^2	0.963	0.968
A	15.30	14.72
B	4.21	6.57
Boyed model $B_t = -0.4978 - \ln(1 - (q_t/q_\infty))$		
R^2	0.79	0.58

the Boyd model support the chemisorption assumptions proposed by Elovich, highlighting the significance of electrostatic interactions and hydrogen bonding in the context of the intra-particle diffusion mechanism associated with the nanosorbent.

3.2.3. Effect of the nanocomposite dose. Fig. 6c illustrates how variations in the mass dose of the N-Bent-NAl_2O_3-NZnO nanosorbent affect the *R*% of the organic contaminants malathion and DDT. It was observed that the *R*% values for the N-Bent-NAl_2O_3-NZnO nanosorbent demonstrated a progressive improvement as the amount of nanosorbent was raised in a solution of malathion and DDT, maintaining an initial pH of 3.0, a concentration of 40 mg L^{-1}, and a reaction duration of 80 min. Initially, the R% values of malathion and DDT exhibited a rapid increase, reaching 40.0 mg in a short period. Subsequently, the rate of increase slowed down as it approached 80.0 mg. Beyond this point, the weight increase was almost completely stabilized. This behavior can be attributed to the relationship between the transfer rate of the adsorbate and the concentration gradient, along with the dynamics of the adsorbent surface exchange.[33] In a different situation, the initial concentrations of malathion and DDT are maintained at a constant rate, while the adsorption efficiency is determined exclusively by the exchange surface. As a result, when the adsorbent dosage is insufficient, the active sites on the surface become saturated and are rendered unavailable for interaction with the adsorbate.[34] With an increase in dosage, additional active binding sites are introduced within the same volume, allowing for increased interaction between the adsorbing species and the nanocomposite. This enhancement raises the chances of molecule–site interactions, thereby facilitating better retention.[33,34] Thus, the maximum adsorption efficiencies were determined to be 94.31% for DDT and 96.97% for malathion, corresponding to a nanocomposite application of 80.0 mg.

3.2.4. Effects of initial concentration of malathion and DDT and isotherm studies. The initial concentration factor significantly affects both the adsorption process and the effectiveness of malathion and DDT removal on N-Bent-NAl_2O_3-NZnO, while also explaining the underlying adsorption mechanism. The relationship illustrated in Fig. 6d shows the initial

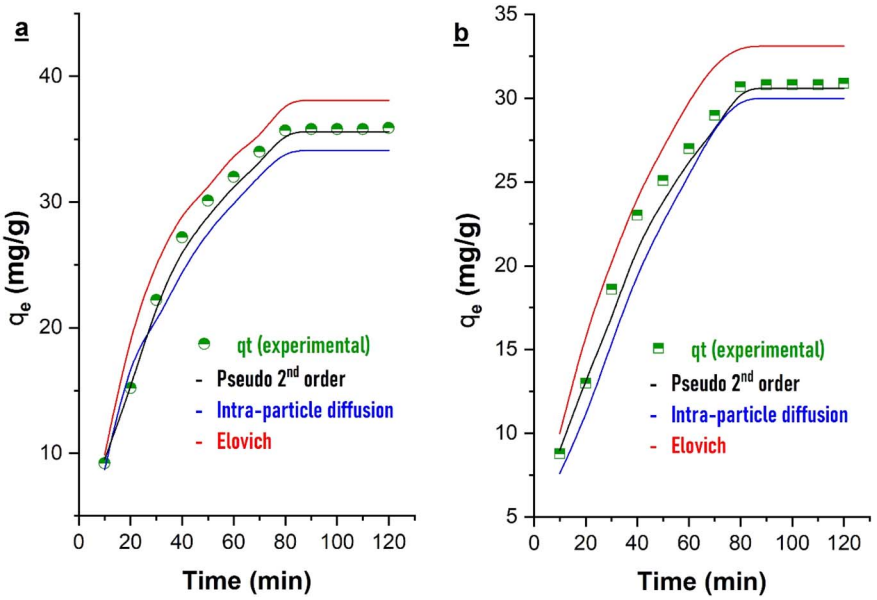

Fig. 7 Kinetics models (Pseudo second order, Intra-particle diffusion and Elovich kinetic model) for (a) malathion and (b) DDT adsorption onto the N-Bent-NAl_2O_3-NZnO nanocomposite at 25 °C.

concentrations of malathion and DDT against the R% values associated with N-Bent-NAl_2O_3-NZnO. It is clear from the figure that malathion achieved higher adsorption efficiencies than DDT across all concentration levels examined. Fig. 6d illustrates that the R% of malathion and DDT by N-Bent-NAl_2O_3-NZnO exhibited a gradual decline, decreasing from 97.67% to 53.71% for malathion and from 95.52% to 48.33% for DDT as the initial concentration rose from 10.0 mg L^{-1} to 120.0 mg L^{-1} for both contaminants. This phenomenon can be explained by the rise in organic pollutant molecules, which exceeds the constant number of surface active sites on N-Bent-NAl_2O_3-NZnO.[33] The elevated sorption levels of the organic pollutants malathion and DDT observed at reduced concentrations may be explained by the more effective interaction between these pollutant molecules in the aqueous solution and the active sites present on the surface of the nanosorbent. Nevertheless, when exposed to elevated concentrations of malathion and DDT, the adsorption performance may be adversely affected due to excessive loading on the adsorptive sites. As the concentration of pollutant molecules rises, the saturation of adsorption sites on N-Bent-NAl_2O_3-NZnO becomes evident, leading to a decrease in adsorption efficiency for the same mass dose of the nanocomposite.[34]

The assessment of the anticipated adsorption behavior of malathion and DDT onto N-Bent-NAl_2O_3-NZnO involves the study of three adsorption isotherm models: Langmuir, Freundlich, and Temkin. The analysis of the isotherm models contributes to a better understanding of the interaction mechanisms between the adsorbates and the adsorbents, while also revealing the sorption capacity of the adsorbents. Table 4 provides a summary of the comparative analysis of the Langmuir, Freundlich, and Temkin isotherm parameters, along with the corresponding non-linear equations for each model. According to the Langmuir model, the surface of the adsorbent is covered by a homogeneous monolayer of the adsorbate. Furthermore, we assumed that the molecules of the adsorbate did not interact.[39] On the other hand, the Freundlich model is an empirical formula that describes a non-ideal and reversible adsorption process on surfaces distinguished by their heterogeneous characteristics. This model uses a multilayer adsorption mechanism, where the initial filling of strong binding sites is influenced by the binding strength, which correlates with the equilibrium concentration.[33] The Temkin isotherm model explains the consistent distribution of binding energies.[35] This suggests that apart from extremely high or low initial concentrations of the adsorbate, a linear decline in the heat of adsorption occurs as the adsorbent becomes more saturated with the adsorbate, as a result of the interactions between the two entities. Moreover, this model is relevant for predicting the adsorption process, whether it is influenced by chemical or physical factors. The values of the Temkin constants, denoted as a_T and b_T, can be identified through the slope and intercept of the corresponding non-linear graph. To define a model that effectively represents the adsorption behavior of malathion and DDT, a graph was generated to show the correlation between the residual levels of the pollutants (C_e, mg L^{-1}) and the adsorption capacity (q_e, mg g^{-1}). The fitting process was performed using the Origin Pro program, as demonstrated in Fig. 8a and b. The analysis revealed a high R^2 value, indicating that the Langmuir model is most appropriate for characterizing the adsorption behavior of malathion and DDT onto N-Bent-NAl_2O_3-NZnO. This result suggests that the adsorption processes for both malathion and DDT onto N-Bent-NAl_2O_3-NZnO can be classified as monolayer and uniformly distributed, with the adsorption forces consistent across these sites.[34] Furthermore, the adsorption capacity, $q_{e(cal)}$, which originates from the non-linear representation of the Langmuir isotherm, closely matches the experimentally determined value, $q_{e(exp)}$. The maximum capacities for the monolayer adsorption of malathion and DDT by the N-Bent-NAl_2O_3-NZnO nanocomposite, denoted as q_{max}, were determined to be 34.20 mg g^{-1} and 28.36 mg g^{-1}, respectively, as detailed in Table 4. In addition, the q_{max} value for malathion is greater than that for malathion, suggesting that N-Bent-NAl_2O_3-NZnO exhibits varying affinities for adsorbing species characterized by distinct molecular structures.[35] The determined K_L values of 0.201 for malathion and 0.219 for DDT indicate that favorable adsorption processes occur between the adsorbed substances (malathion and DDT) and the N-Bent-NAl_2O_3-NZnO nanosorbent at a pH level of 3.0. In addition to examining the interaction mechanism between the adsorbate and adsorbent on the surface of the nanocomposite, the heat of adsorption was analyzed using the Temkin model, as it effectively characterizes the adsorption processes of malathion and DDT in recent studies. The Temkin model indicates a progressive rise in the heat of

Table 4 Adsorption isotherm models and their parameters for the removal of malathion and DDT using the N-Bent NAl_2O_3-NZnO nanocomposite

Parameter	Malathion	DDT
Langmuir isotherm model $C_e/q_e = 1/bq_m + C_e/q_m$		
q_{max}	34.20	28.36
$q_{e(exp)}$	35.80	31.34
R^2	0.997	0.991
K_L[a]	0.201	0.219
q_m	26.36	30.20
Freundlich isotherm model $\ln q_e = \ln K_F + 1/n \ln C_e$		
R^2	0.916	0.908
n_F[a]	4.35	6.07
q_e	7.47	5.98
K_F[a]	0.41	0.29
Temkin isotherm model $q_e = (RT/b_T)\ln a_T + (RT/b_T)\ln C_e$		
R^2	0.974	0.919
a_T[a]	227	304

[a] K_L (L mg^{-1}) is the Langmuir constant related to the maximum monolayer adsorption capacity and adsorption energy. n_F is the Freundlich constant related to the adsorption intensity (heterogeneity factor). K_F is the Freundlich constant related to the adsorption capacity (heterogeneous layer capacity). a_T is the Temkin isotherm constant in L g^{-1}. b_T is the Temkin constant related to the heat of adsorption in J mol^{-1}. R is the gas constant (8.314 J mol^{-1} K^{-1}). T is the absolute temperature in Kelvin.

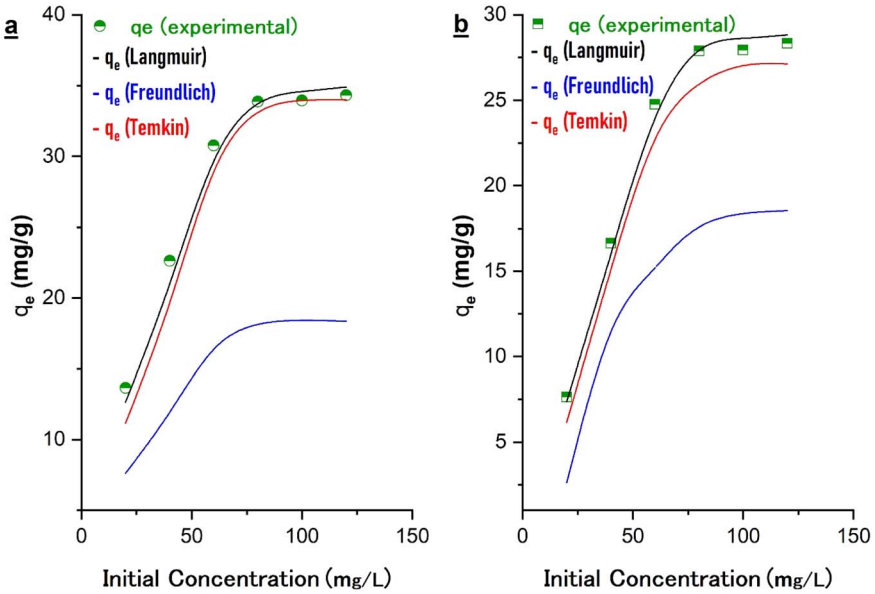

Fig. 8 Langmuir, Freundlich and Temkin isothermal models for (a) malathion and (b) DDT adsorption onto the N-Bent-NAl_2O_3-NZnO nanocomposite at 25 °C.

adsorption corresponding to the enlargement of the surface area of the N-Bent-NAl_2O_3-NZnO nanocomposite.

3.2.5. Desorption and recyclability. From a practical application perspective, the recyclability of advanced absorbents is of paramount importance. The reason for this is that the ability to reuse these materials directly affects their cost-effectiveness and overall sustainability. The reusability and stability of N-Bent-NAl_2O_3-NZnO were assessed through a series of adsorption–desorption-re-adsorption processes, which were carried out at room temperature over five consecutive cycles. The R% values for each cycle were assessed and are displayed in Fig. 9. The reactions were performed under the identical experimental conditions outlined earlier. Following each cycle, the entire mass of the N-Bent-NAl_2O_3-NZnO nanocomposite was collected, subjected to multiple washings with a methanol and acetic acid mixture, air-dried at ambient temperature, and subsequently employed in the next cycle to remove the two targeted organic contaminants. The recorded *R*% values were standardized based on the *R*% from the first cycle. The data indicate that the adsorption capacity of N-Bent-NAl_2O_3-NZnO experienced a decline with the rise in the number of cycles for both types of organic pollutants. This reduction is likely a consequence of the compromised pore structure and the decrease in adsorption sites, which occurred due to the agglomeration of the absorbents. Additionally, the insufficient elution of the selected organic pollutant molecules from the nanocomposite may have played a role in this phenomenon.[39] The results at the end of the first cycle indicate removal efficiencies of 97.51% for malathion and 95.02% for DDT. After four cycles, the maximum adsorption efficiency of malathion was 91.2% and that of DDT was 90.10%. Upon reaching cycle number five, a notable decline in the malathion removal rate was noted, which decreased by 12.88% to a total of 84.63%. In parallel, the removal of DDT experienced a reduction of approximately 13.26%, resulting in a final efficiency of 81.76%. This suggests that N-Bent-NAl_2O_3-NZnO could be reused to a certain extent. Similar results have been obtained in relevant studies.[11,35] Despite these negative effects, N-Bent-NAl_2O_3-NZnO maintains its effective remediation performance against malathion and DDT pesticides and exhibits good reusability, making it an effective adsorbent for the remediation of polluted wastewater.

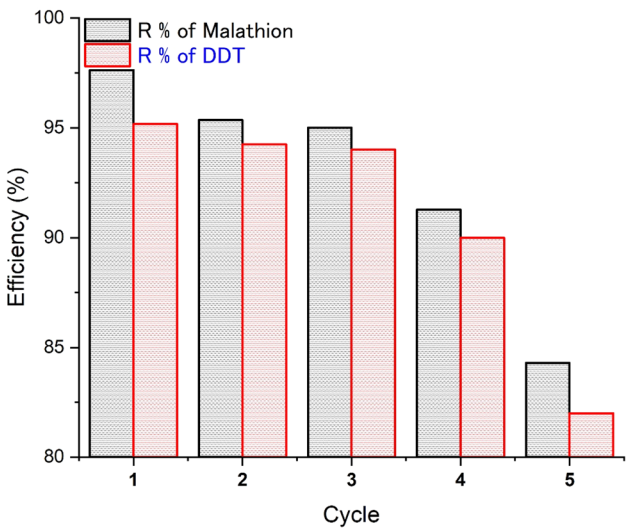

Fig. 9 Different reusability cycles of the N-Bent-NAl_2O_3-NZnO nanocomposite for malathion and DDT adsorption at the contact time of 80 min, initial pH value of 3.0, initial concentration of 40.0 mg L^{-1} and shaking speed of 240 rpm.

4. Conclusions

In this study, the applicability of the batch adsorption process in removing malathion and DDT pesticides from contaminated wastewater by the newly assembled N-Bent-NAl_2O_3-NZnO nanocomposite was investigated. This nanocomposite achieved remarkable removal efficiencies of 97.42% and 94.83% for malathion and DDT, respectively, under optimal experimental conditions. In all the tested factors, malathion exhibited higher overall removal efficiency than DDT. For both pesticide pollutants, the adsorption behavior was most effectively described by pseudo second order kinetics. Compared to the other studied isotherm models, the Langmuir isotherm provided a favorable alignment with the experimental data of both pesticides onto N-Bent-NAl_2O_3-NZnO, suggesting a chemisorption process and monolayer adsorption. The reusability test assessment of N-Bent-NAl_2O_3-NZnO indicated a reasonably high removal efficiency of both pesticide pollutants after five regeneration processes. The findings of this study indicate that N-Bent-NAl_2O_3-NZnO is an efficient, sustainable and affordable nanocomposite with promising potential for removing organochlorine and organophosphorus pesticides from aqueous environments. However, the limitations of the proposed method could be correlated to the maximum identified removal capacity values by the Langmuir model, as 34.20 mg g^{-1} for malathion and 28.36 mg g^{-1} for DDT. Therefore, the adsorption efficiency is somewhat low and may need to be increased by incorporating other effective functional groups and this will be the subject of our future work.

Data availability

The authors confirm that the data used to support the findings of this study are included in the article.

Conflicts of interest

There are no conflicts to declare.

References

1 W. J. Cosgrove and F. R. Rijsberman, *World Water Vision: Making Water Everybody's Business*, Routledge, 2014.
2 A. Abdelfattah, S. S. Ali, H. Ramadan, E. I. El-Aswar, R. H. S. H. Eltawab, T. Elsamahy, S. Li, M. M. El-Sheekh, M. Schagerl, M. Kornaros and J. Sun, Microalgae-based wastewater treatment: mechanisms, challenges, recent advances, and future prospects, *Environ. Sci. Ecotechnology*, 2022, **13**, 100205.
3 D. R. Wallace and A. B. Djordjevic, Heavy metal and pesticide exposure: A mixture of potential toxicity and carcinogenicity, *Curr. Opin. Toxicol.*, 2020, **19**, 72–79.
4 B. B. Lin, Resilience in agriculture through crop diversification: adaptive management for environmental change, *BioScience*, 2011, **61**, 183–193.
5 A. Zapata, S. Malato, J. A. Sanchez-Perez, I. Oller and M. I. Maldonado, Scale-up strategy for a combined solar photo-Fenton/biological system for remediation of pesticide-contaminated water, *Catal. Today*, 2010, **151**, 100–106.
6 M. H. Hashimi and R. H. Q. Ryan, Toxic effects of pesticides on humans, plants, animals, pollinators and beneficial organisms, *Asian Plant Res. J.*, 2020, **5**, 37–47.
7 R. Cech, J. G. Zaller, A. Lyssimachou, P. Clausing, K. Hertoge and C. Linhart, Pesticide drift mitigation measures appear to reduce contamination of non-agricultural areas, but hazards to humans and the environment remain, *Sci. Total Environ.*, 2023, **854**, 158814.
8 *The WHO Recommended Classification of Pesticides by Hazard and Guidelines to Classification Citation: International Program on Chemical Safety*, World Health Organization, WHO Press, World Health Organization, Geneva, Switzerland, 2009.
9 J. Ruzzin, Public health concern behind the exposure to persistent organic pollutants and the risk of metabolic diseases, *BMC Public Health*, 2012, **12**, 298.
10 R. Carson, *Silent Spring*, Mariner Books Pub, 1962.
11 R. R. Kalantary, A. Azari, A. Esrafili, K. Yaghmaeian, M. Moradi and K. Sharafi, The survey of malathion removal using magnetic graphene oxide nanocomposite as a novel adsorbent: thermodynamics, isotherms, and kinetic study, *Desalin. Water Treat.*, 2016, **57**, 8460–28473.
12 Y. Ning, K. Li, Z. Zhao, D. Chen, Y. Li, Y. Liu, Q. Yang and B. Jiang, Simultaneous electrochemical degradation of organophosphorus pesticides and recovery of phosphorus: synergistic effect of anodic oxidation and cathodic precipitation, *J. Taiwan Inst. Chem. Eng.*, 2021, **125**, 267–275.
13 S. Poomagal, R. Sujatha, P. S. Kumar and D. V. N. Vo, A fuzzy cognitive map approach to predict the hazardous effects of malathion to environment (air, water and soil), *Chemosphere*, 2021, **263**, 127926.
14 W. Li, Y. Zhao, X. Yan, J. Duan, C. P. Saint and S. Beecham, Transformation pathway and toxicity assessment of malathion in aqueous solution during UV photolysis and photocatalysis, *Chemosphere*, 2019, **234**, 204–214.
15 Y. Vasseghian, M. Moradi, M. Pirsaheb, A. Khataee, S. Rahimi, M. Y. Badi and A. M. Khaneghah, Pesticide decontamination using UV/ferrous-activated persulfate with the aid neuro-fuzzy modeling: a case study of malathion, *Food Res. Int.*, 2020, **137**, 109557.
16 Q. Lao, G. Liu, X. Zhou, F. Chen and S. Zhang, Sources of polychlorinated biphenyls (PCBs) and dichlorodiphenyltrichloroethanes (DDTs) found in surface sediment from coastal areas of beibu gulf: a reflection on shipping activities and coastal industries, *Mar. Pollut. Bull.*, 2021, **167**, 112318.
17 M. A. El-Sheikh, T. Hadibarata, A. Yuniarto, P. Sathishkumar, E. M. Abdel-Salam and A. A. Alatar, Role of nanocatalyst in the treatment of organochlorine compounds - a review, *Chemosphere*, 2021, **268**, 128873.
18 P. Gong, H. Xu, C. Wang, Y. Chen, L. Guo and X. Wang, Persistent organic pollutant cycling in forests, *Nat. Rev. Earth Environ.*, 2021, **2**, 182–197.

19 I. U. Keru, A. K. Geletu and K. T. Wondimu, Multi residue analysis of persistent organochlorine pesticides in fish from Baro River, Gambella, Southwest Ethiopia, *Reg. Stud. Mar. Sci.*, 2023, **66**, 103126.
20 M. M. S. Sanad, S. E. Gaber, E. I. El-Aswar and M. M. Farahat, Graphene-magnetite functionalized diatomite for efficient removal of organochlorine pesticides from aquatic environment, *J. Environ. Manage.*, 2023, **330**, 117145.
21 Y. Liu, X. Ji, Z. Gao, Y. Wang, Y. Zhu, Y. Zhang, Y. Zhang, H. Sun, W. Li and J. Duan, Adsorption characteristics and removal mechanism of malathion in water by high and low temperature calcium–modified water hyacinth–based biochar, *J. Cleaner Prod.*, 2023, **411**, 137258.
22 W. Studzinski, I. Narloch and Ł. Dąbrowski, Determination of the efficiency of electrolyzed water devices for the removal of pesticides in aqueous solutions and the characteristics of the pesticide residues and their transformation products, *J. Water Process Eng.*, 2024, **61**, 105372.
23 W. Cao, Y. Qi, Y. Zhang, R. Guo, R. Qu and Z. Wang, Insight into the photodegradation of o,p'-dichlorodiphenyltrichloroethane in a broad spectrum of irradiation light, *Chem. Eng. J.*, 2024, **488**, 150855.
24 A. H. S. Júnior, C. R. S. Oliveira, T. W. Leal, A. B. Mapossa, J. Fiates, A. A. U. Souza, S. M. A. G. Ulson de Souza and A. Silva, Organochlorine pesticides remediation techniques: Technological perspective and opportunities, *J. Hazard. Mater. Lett.*, 2024, **5**, 100098.
25 D. Danilian, F. M. Bundrück, A. Kikas, T. Käämbre, H. Mändar, S. Lehner, A. Gogos, J. Kozlova, M. Kook, V. Kiisk, J. Link, R. Stern, A. Ivask, V. Kisand and R. Pärna, Reusable magnetic mixture of $CuFe_2O_4$–Fe_2O_3 and TiO_2 for photocatalytic degradation of pesticides in water, *RSC Adv.*, 2024, **14**, 12337–12348.
26 P. Kajitvichyanukul, V. H. Nguyen, T. Boonupara, L. A. P. Thi, A. Watcharenwong, S. Sumitsawan and P. Udomkun, Challenges and effectiveness of nanotechnology-based photocatalysis for pesticides-contaminated water: A review, *Environ. Res.*, 2022, **212**, 113336.
27 M. A. Sandoval, J. Vidal, W. Calzadilla and R. Salazar, Solar (electrochemical) advanced oxidation processes as efficient treatments for degradation of pesticides, *Curr. Opin. Electrochem.*, 2022, **36**, 101125.
28 X. Zhang, L. Wang, M. Quinto, X. Jin, Y. Zou, J. Ge, H. Liu and D. Li, A new sustainable filtration membrane extraction method based on nanoconfined liquid phase extraction: Determination of organochlorinated pesticides and pyrethroids in tea samples, *Anal. Chim. Acta*, 2024, **1307**, 342624.
29 M. B. M. Y. Ang, C. A. Trilles, M. R. D. Guzman, J. M. Pereira, R. R. Aquino, S. H. Huang, C. C. Hu, K. R. Lee and J. Y. Lai, Improved performance of thin-film nanocomposite nanofiltration membranes as induced by embedded polydopamine-coated silica nanoparticles, *Sep. Purif. Technol.*, 2019, **224**, 113–120.
30 O. G. Júnior, M. G. B. Santos, A. B. S. Nossol, M. Clara, V. M. Starling and A. G. Trovó, Decontamination and toxicity removal of an industrial effluent containing pesticides via multistage treatment: Coagulation-flocculation-settling and photo-Fenton process, *Process Saf. Environ. Prot.*, 2021, **147**, 674–683.
31 J. Venkatachalam, H. Mohan and K. K. Seralathan, Significance of *Herbaspirillum* sp. in biodegradation and biodetoxification of herbicides, pesticides, hydrocarbons and heavy metals – A review, *Environ. Res.*, 2023, **239**, 117357.
32 Z. Shamsollahi and A. Partovinia, Recent advances on pollutants removal by rice husk as a bio-based adsorbent: a critical review, *J. Environ. Manage.*, 2019, **246**, 314–323.
33 R. M. El-Sharkawy, E. A. Allam, A. S. M. Ali and M. E. Mahmoud, Adsorption study of bisphenol-A and chlorpyrifos onto nanobentonite intercalated with magnetite and sodium alginate: kinetics and isotherm models, *Int. J. Sci. Environ. Technol.*, 2022, **19**, 9827–9842.
34 E. A. Allam, A. S. M. Ali, R. M. Elsharkawy and M. E. Mahmoud, Framework of nano metal oxides N-NiO@N-Fe_3O_4@N-ZnO for adsorptive removal of atrazine and bisphenol-A from wastewater: Kinetic and adsorption studies, *Environ. Nanotechnol., Monit. Manage.*, 2021, **16**, 100481.
35 M. E. Mahmoud, R. M. El-Sharkawy and G. A. A. Ibrahim, A novel bionanocomposite from doped lipase enzyme into magnetic graphene oxide-immobilized-cellulose for efficient removal of methylene blue and malachite green dyes, *J. Mol. Liq.*, 2022, **368**, 120676.
36 S. Hua, J. L. Gong, G. M. Zeng, F. B. Yao, M. Guo and X. M. Ou, Remediation of organochlorine pesticides contaminated lake sediment using activated carbon and carbon nanotubes, *Chemosphere*, 2017, **177**, 65–76.
37 M. A. Habila, Z. A. Alothman, S. A. Al-Tamrah, A. A. Ghafar and M. Soylak, Activated carbon from waste as an efficient adsorbent for malathion for detection and removal purposes, *J. Ind. Eng. Chem.*, 2015, **32**, 336–344.
38 R. Kumar, L. George, Z. Jun and S. Mukherji, Photocatalytic activity of graphene oxide-TiO_2 nanocomposite on dichlorvos and malathion and assessment of toxicity changes due to photodegradation, *Chemosphere*, 2022, **308**, 136402.
39 S. Ullah, H. Nasir, T. Akhtar, S. Mahboob, S. A. B. Bukhari and K. H. Thebo, Efficient removal of the organophosphate pesticide, profenofos using polymer-stabilized microporous Fe_2O_3-ZnO nanocomposite: Kinetic and thermodynamic analysis, *Appl. Surf. Sci.*, 2024, **662**, 160027.
40 R. M. El-Sharkawy, E. A. Allam and M. E. Mahmoud, Functionalization of CeO_2-SiO_2-$(CH_2)_3$-Cl nanoparticles with sodium alginate for enhanced and effective CdII, PbII, and ZnII ions removal by microwave irradiation and adsorption technique, *Environ. Nanotechnol. Monit. Manag.*, 2020, **14**, 100367.
41 H. Qin, L. Xu, L. Qin, B. Kang, F. Zha, Q. Wang and K. Huang, Removal of Cu(II) by sodium hexametaphosphate and nano zero-valent iron modified calcium bentonite: characteristic, adsorption performance and mechanism, *J. Environ. Manage.*, 2024, **358**, 120866.

42 M. E. Mahmoud, M. A. Khalifa, M. R. Youssef and R. M. El-Sharkawy, Comparative morphological, thermal, and mechanical characteristics of doped bentonite and dolomite natural clay fillers into high-density polyethylene, *J. Appl. Polym. Sci.*, 2024, **141**, e55875.

43 F. Zahaf, R. Marouf, F. Ouadjenia and J. Schott, Kinetic and thermodynamic studies of the adsorption of Pb(II), Cr(III) and Cu(II) onto modified bentonite, *Desalin. Water Treat.*, 2018, **131**, 282–290.

44 M. M. Rahman, M. S. Yeasmin, M. J. Uddin, M. Hasan, M. A. A. Shaikh, M. S. Rahman and M. Maniruzzaman, Simultaneous abatement of Ni^{2+} and Cu^{2+} effectually from industrial wastewater by a low cost natural clay-chitosan nanocomposite filter: Synthesis, characterization and fixed bed column adsorption study, *Environ. Nanotechnol. Monit. Manag.*, 2023, **20**, 100797.

45 R. Naseem and S. S. Tahir, Removal of Fe(II) from the wastewater of galvanized pipe manufacturing industry by adsorption onto bentonite clay, *J. Environ. Manage.*, 2004, **73**, 285–292.

46 S. S. Tahir and R. Naseem, Removal of Cr(III) from tannery wastewater by adsorption onto bentonite clay, *Sep. Purif. Technol.*, 2007, **53**, 312–321.

47 M. E. Mahmoud, M. A. Khalifa, R. M. El-Sharkawy and M. R. Youssef, Effects of Al_2O_3 and BaO nano-additives on mechanical characteristics of high-density polyethylene, *Mater. Chem. Phys.*, 2021, **262**, 124251.

48 M. E. Mahmoud, M. A. Khalifa, M. R. Youssef and R. M. El-Sharkawy, Influence of MgO and ZnO as nano-additives on the mechanical, microstructural and thermal performance of high-density polyethylene, *J. Appl. Polym. Sci.*, 2022, **139**, e52705.

49 A. Sedigheh, H. Raissi and A. Zaboli, Adsorption Efficiency of Carbon Materials for the Removal of Organic Pollutants: DDT from Aqueous Solution, *J. Phys. Chem. B*, 2023, **127**, 10518–10528.

50 A. Ketiyala and L. Jamir, *Application of Activated Carbon and Its Modifications in Wastewater Treatment, Aerobic and Anaerobic Microbial Treatment of Industrial Wastewater*, CRC Press, pp. 167–185.

51 K. Suman, Strategic synthesis of biowaste-derived magnetic hydrochar for adsorption and photocatalytic removal of Chlorpyrifos herbicides from simulated wastewater, *Mater. Sci. Eng. B*, 2025, **314**, 118009.

52 V. Milanković, T. Tasić, S. Brković, N. Potkonjak, C. Unterweger, D. Bajuk-Bogdanović, I. Pašti and T. Lazarević Pašti, Spent coffee grounds-derived carbon material as an effective adsorbent for removing multiple contaminants from wastewater: A comprehensive kinetic, isotherm, and thermodynamic study, *J. Water Process Eng.*, 2024, **63**, 105507.